AIAA SciTech
13-17 January 2014, National Harbor, Maryland
52nd Aerospace Sciences Meeting

FULL-ANNULUS SIMULATION OF NON-SYNCHRONOUS BLADE VIBRATION EXCITATION OF AN AXIAL COMPRESSOR

Daniel Espinal *
Hong-Sik Im†
Ge-Cheng Zha‡
Dept. of Mechanical and Aerospace Engineering
University of Miami
Coral Gables, Florida 33124
E-mail: gzha@miami.edu

ABSTRACT

A high speed 1-1/2 axial compressor stage is simulated in this paper using an Unsteady Reynolds-Averaged Navier-Stokes (URANS) solver for a full-annulus configuration to capture its non-synchronous vibration (NSV) flow excitation. The simulation presented in this paper assumes rigid blades. A 3rd order WENO scheme for the inviscid flux and a 2nd order central differencing for the viscous terms are used to resolve nonlinear interaction between blades and fluid flow. A fully conservative rotor/stator sliding boundary condition is employed with multiple-processor capability for rotor/stator interface information exchange for parallel computing. The sliding BC accurately captures unsteady wake propagation between the rotor and stator blades while conserving fluxes across the rotor/stator interfaces. The predicted dominant frequencies using the blade tip response signals are not harmonic to the engine order, which is the NSV excitation. The simulation is based on a rotor blade with a 1.1% tip-chord clearance. Comparison to previous 1/7th annulus simulations show previous time-shifted phase-lag BCs are accurate. The NSV excitation frequency of the full annulus simulation is for the most part 3.3% lower than experimental and matches with the 1/7th annulus simulation, although some blades displayed slightly different NSV excitation frequencies. The full annulus simulation confirms that the instability of tornado vortices in the vicinity of the rotor tip due to the strong interaction of incoming flow, tip vortex and tip leakage flow is the main cause of the NSV excitation. This instability is present in all blades of the rotor annulus. While the time-shifted phase lag BCs can accurately capture the frequency of NSV excitation, phenomena related to flow separation with lower frequencies, including dual-vortex systems within blade passages, are not captured by the 1/7th annulus simulation, but are found in the full-annulus simulation.

Nomenclature

e	total energy per unit mass
L_∞	blade chord at hub
N_B	number of blade
N_D	number of nodal diameter
p	static pressure
R_o	Rossby number, $\frac{\Omega L_\infty}{U_\infty}$
r	radius
T	period for one nodal diameter

*Ph.D. Student
†Ph.D., Currently an engineer at Honeywell
‡Professor.

U, V	velocities in x, y direction
U_∞	inlet axial velocity
V_x, V_θ, V_r	absolute velocities in x, θ, r direction
W_θ	relative velocity in θ direction
$\tilde{\nu}$	working variable of the S-A model related to turbulent eddy viscosity
Ω	rotor angular speed in *radians/sec*
ϕ	inter blade phase angle(IBPA), $\frac{2\pi \cdot N_D}{N_B}$
ρ	fluid density

BC	boundary condition
BPF	blade passing frequency
IGV	inlet guide vane
NSV	non-synchronous vibration
RI	rotating instability
URANS	unsteady Reynolds-averaged Navier-Stokes
CUSP	Convective Upwind and Splitting Pressure
WENO	Weighted Essentially Non-oscillatory
LE	Leading Edge
TE	Trailing Edge

1 Introduction

Turbomachinery aeromechanic problems are very challenging since they involve both aerodynamics and structural vibration. Blade vibration due to forced response and flutter have been studied for decades with the progress of improving turbomachinery efficiency and reliability. Recently, a new turbomachinery aeromechanic problem, namely non-synchronous vibration (NSV), whose blade vibration frequency is away from harmonics of rotor shaft frequency, has attracted a lot of attention [1–8].

Rotating Instability (RI) is considered as one cause of NSV [1–4]. The experiment by Baumgartner et al. [1] shows that for a certain operating condition high vibration levels on the first stage blades exist. The frequencies are not in resonance with engine orders. A rotating flow instability revolves relative to the blade row similar to rotating stall cell. The velocity fluctuations measured by the Hot-film probe near the blade trailing edge show the radial dependency of this rotating instability. The frequencies of the rotating instability are visible at 91% blade span with high coherence levels. The levels are dying away from the RI center, and eventually at 65% blade span the RI is no more detectable.

Kielb et al. [2] conducted an experimental and numerical investigation for a full size compressor rig where blade-mounted strain gages and case-mounted unsteady pressure transducers are devised to measure the NSV. The experimental strain gage data show step change in frequency as the compressor operating condition varies, which is another feature of the NSV. The stage 1 rotor blades experience a significant NSV response of 2661 Hz at 12700 rpm near first torsional mode (1T) and exhibit the NSV frequency shift from 2661 to 2600 Hz at 12800 rpm. While at the casing, the NSV frequencies of 3516 Hz and 3662 Hz are measured in the non-rotating reference frame. Their numerical results for the 1/7th rotor annulus rotor indicate a suction side vortex shedding and a tip flow instability near 75% span as the excitation source of the NSV.

The work of Marz et al. [3] also shows the rotating instability as the main source for NSV. A low speed single stage fan with outlet guide vanes is used for their experimental and numerical study on NSV. The rotor design speed is 3000 rpm and has the blade passing frequency (BPF) of 560 Hz. They tested four different tip clearances of 0.7%, 1.4%, 2.8%, and 5.6% tip axial chord at near the maximum fan loading condition. The measured wall pressure spectrum shows a NSV frequency at roughly half of BPF. The time-lapse plots of casing wall pressure indicate that the flow intensity varies from blade to blade with the presence of a high fluctuating flow instability in the rotor entry plane for tip clearances of 2.8% and 5.6%. It turns out that the blade sensor signal near the rotating instability has a strong periodic content. A vortex structure moving from the suction side to the pressure side is observed in the middle of the blade passage by the full annulus simulation for 2.8% tip model, which is the main causes of unsteadiness when the rotating instability develops. The numerical study shows no tip spillage flow even with the rotating instability.

Mailach et al. [4] carried out an experimental study of a low speed research compressor to investigate influence of tip clearance and operating point on rotating instability. Rotating instability have been found at a tip clearance of 3% tip axial chord. At a larger tip clearance of 4.3%, the rotating instability is fully developed for all the rotor speeds including 50%, 80%, and 100% design speed. The formation of rotating instability is limited to a narrow operating range near the stall boundary. The measurement at the casing wall shows a narrow band increase of the amplitudes in the frequency spectrum at about 30% of BPF. When the compressor approaches the stall boundary, the rotating instability shifts to slightly lower frequencies while amplitude of the perturbation grows. Measurements on the rotor blades show that the rotating instability is

limited to the blade tip region. Maximum amplitudes appear at 92% of the blade height and 20% to 30% of chord length. For a large tip clearance a strong blade tip vortex is observed in the rotor tip region. The fluctuating blade tip vortices propagate in rotor circumferential direction. Tip clearance size is shown as the main influence parameter on the rotating instability.

Thomassin et al. [5, 6] suggested a theory different from the rotating instability to explain the NSV based on the resonance of a impinging jet vortex structure and the acoustic feedback of a vibrating plate. The jet core feedback theory has been proved by an experiment conducted in [5, 6]. It shows that when the acoustic reflection wave length equals to the jet-to-plate distance, the jet vortical structures lock-on to the acoustic wave frequency and significant amplification of the pressure fluctuation and vibration of the flexible plate are observed. They suggest a simple model to predict the critical tip velocity based on their impinging jet experiment, which is tested in this study to evaluate the effect of tip leakage jet acoustics on NSV of the compressor under investigation. Vo [8]'s simulation shows a tip clearance flow instability for an isolated subsonic axial compressor rotor. In the blade tip region the trailing edge backflow causes flow impingement on the pressure side that leads to the flow unsteadiness associated with NSV.

A NSV phenomenon for a low aspect ratio fan stage stator with a large amplitude is identified by the experiment of Sanders [7]. The rotor blades ahead the stators experience flutter, not NSV. Strain gage measurements on selected vanes at various locations around the annulus show that the highest response occurs on the vicinity of low static pressure(high Mach number) regions of the fan stator assembly. The high amplitude frequencies observed along the nominal operating line during the fan engine test is a narrow band and non-synchronous with the 1st bending mode approximately 25% below. The URANS simulation demonstrates that the NSV is driven by dynamic stalling of the fan stator due to unsteady shock-boundary layer interaction.

A high-speed axial compressor is adopted in this study, which exhibits a strong non-engine order vibration of the 1st stage rotor blades close to the blade 1T (1st torsional) mode during engine tests [2], see Fig. 1. The NSV frequency collapses between 2600 Hz and 2661 Hz with a large amplitude, which is considered as a lock-in phenomenon [9]. Under NSV, no resonance appears but failure of the blade structure such as high cycle fatigue (HCF) can occur. The NSV frequency is shifted from 2600 Hz to 2661 Hz as the rotor speed slightly decreases roughly from 12800 RPM to 12700 RPM. The experiment [2] confirms the NSV occurrence before stall. The rotor tip clearance of the full compressor rig is about 1.1% of tip chord.

Previous efforts by Im et al. [10] have adopted a 1/7th sector of the full-annulus configuration to simulate the first 1-1/2 stages of this compressor due to geometric periodicity. Since NSV is primarily an unsteady phenomenon, to enforce flux conservation across rotor/stator interfaces, a fully conservative sliding boundary condition (BC) was adopted. Because the circumferential boundaries are only geometrically periodic, the flow was treated at these boundaries with a time-shifted phase-lag BC to capture more accurately the physical phenomena inside the compressor. Even though the accuracy of phase-lag BCs is still in question and require more validation, there has not been any full-annulus simulations thus far aimed at predicting NSV.

Full-annulus simulations have been used to explain the flow mechanisms of stall inception since the flow has no circumferential periodicity [11–15]. Due to the unsteadiness of complex flow phenomena in turbomachines, the limitations brought by periodicity assumptions must be overcome in order to resolve more realistically flow structures. Since the knowledge on NSV excitation is very limited, there are some questions that need to be answered: 1) is NSV excitation a full annulus phenomenon or a local phenomenon? 2) What are the NSV excitation characteristics along the circumference, periodic or aperiodic? Only a full annulus simulation can answer these questions. The answer is also very important to guide the reduced model using a sector of the annulus. In [10] a tornado vortex structure near the rotor blade tip region was found to be the main flow structure to drive the NSV for the present compressor. The vortex structure observed from the 1/7 sector simulation for this compressor stage suggests that the tornado vortex structure is present in all the rotor passages of the annulus, effectively creating a vortex tube that may span the full circumference of the rotor blade-row. Therefore, a 1/7th annulus model is not sufficient to test the order of length scale this vortex structure requires and a full-annulus model is warranted.

The purpose of this study is to present a high-fidelity simulation of the NSV aerodynamic excitation in the first 1-1/2 stages of the high-speed axial compressor using a full-annulus configuration to capture flow structures with length scales on the order of the rotor circumference and to prevent errors induced due to circumferential BCs. Also, the current study will aid in the validation of the time-shifted phase-lag BC adopted by Im et al. [10] by comparing the results of the 1/7th annulus simulations to the full-annulus results.

2 The High-Speed Axial Compressor

The high-speed axial compressor exhibits NSV at the first stage rotor blades [2]. The first 1-1/2 stage with 56 IGVs, 35 rotor blades and 70 stator blades of the full compressor is used for current simulations. The rotor tip clearance of the compressor rig is 1.1% of tip chord. The measured blade NSV is a phase-locked response and close to 1st torsional blade natural frequency. The strain gage on the blade surface shows the NSV frequency of 2600 Hz at around 12880 rpm and 2661 Hz as the rotor speed slightly decreases to 12700 rpm as shown in Fig. 1 (left). The measured NSV frequency of the blade surface can be used for comparison since the rotating frame of reference is adopted in this study. Also at the right of Fig. 1 is shown the casing unsteady pressure measurement frequencies in absolute frame, which are doppler shifted. In these pressure

measurements the presence of SFV frequencies is stronger in the rpm range where NSV is present than SFV frequencies in the strain gage measurements.

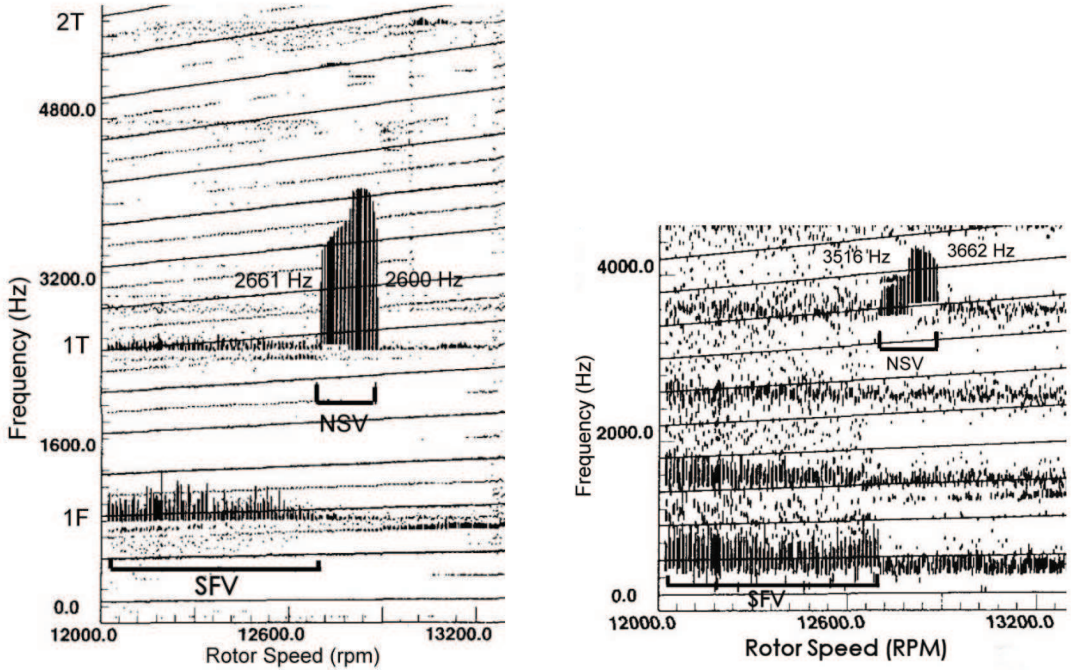

FIGURE 1: Strain gage response (left) and casing unsteady pressure measurements (right) of the first-stage rotor blades of the high-speed compressor showing SFV(separated flow vibration) and NSV(non-synchronous vibration)

3 Numerical Methods

The unsteady Reynolds-averaged Navier-Stokes (URANS) equations are solved in a rotating frame [13] with the Spalart-Allmaras (S-A) turbulence model [16]. Shock capturing scheme is necessary to simulate high-speed axial compressors since most rotor blades experience shock/boundary layer interaction. In this study the Low Diffusion E-CUSP (LDE) Scheme [17] as an accurate shock capturing Riemann solver is used with a 3rd order WENO reconstruction for inviscid flux and a 2nd order central differencing for viscous terms [18]. An implicit 2nd order dual time stepping method [19] is solved using an unfactored Gauss-Seidel line iteration to achieve high convergence rate. The high-scalability parallel computing is implemented to save wall clock time [20].

The interaction between rotating and stationary blades introduces inherent unsteadiness to the flow of multistage turbomachinery. For instance, the shock wave interaction between the inter blade rows as well as rotating instabilities as a main driver of NSV can be predicted not by the steady approach, but only by the conservative unsteady approach. Numerous studies on the unsteady rotor/stator interaction has been developed [21–24] based on interpolation on the rotor-stator interface. Rai [21] used the patched and overlaid grid system based on interpolation to solve an axial turbine with a rotor-stator configuration. Chen et al. [25] pointed out that lack of flux conservation can significantly affect the solution accuracy where shock interaction exists between the blade rows. In fact, the methods of rotor/stator interaction using any type of interpolation methods can not satisfy the conservation of the flux across the interface.

In this study a fully conservative sliding boundary condition (BC) for multiple processors at the blade row interface is developed in order to rigorously resolve wake propagation, shock interactions and rotating instabilities while maintaining an even computational load for the full-annulus simulation.

4 Boundary Conditions

At the IGV inlet, the radial distributions of total pressure, total temperature, swirl angle and pitch angle are specified and velocity is extrapolated from the computational domain in order to determine the rest of the variables. On the blade surface and casing wall a non-slip boundary condition is applied, while on the hub surface the law of the wall is used to avoid an excessive fine mesh in the boundary layer [13]. At the stator outlet, the static pressure is specified in the spanwise direction.

The velocity components are extrapolated from the computational domain and an isentropic relation is used to determine density. If the wall surface is rotating, the wall static pressure for the inviscid momentum equation is determined by solving the radial equilibrium equation. If the wall surface is stationary, the static pressure gradient across the wall boundary is set to zero. In addition, the adiabatic condition is used to impose zero heat flux through the wall.

4.1 Sliding BC Between a Rotor and a Stator

A fully conservative sliding BC without interpolation is used to solve the moving rotor in the rotating frame and the stator blades in the fixed frame [26]. The following relations between the moving frame and the fixed frame are used for variable exchange.

$$\begin{pmatrix} \rho \\ \rho U \\ \rho V_r \\ \rho V_\theta \\ \rho e + \rho V_\theta r R_o \\ \rho \tilde{\nu} \end{pmatrix}_{Fixed} \rightleftharpoons \begin{pmatrix} \rho \\ \rho U \\ \rho V_r \\ \rho W_\theta (= V_\theta - r R_o) \\ \rho e \\ \rho \tilde{\nu} \end{pmatrix}_{Moving} \tag{1}$$

The conservative variables in cylindrical rotating coordinates $\rho, \rho U, \rho V_r, \rho W_\theta$, ρe, and $\rho\tilde{\nu}$ are exchanged dynamically when the moving domains slide and are updated in every pseudo time step. Since the sliding BC with the ghost cell approach can ensure the boundary cells to be solved in the same manner as the inner domain, it hence can capture the interactive effects between the rotor and the stator.

The condition for this sliding BC to avoid interpolation across the sliding BC is to use a one-to-one matched grid at the interface [26]. Two domains at the interface have to have the same mesh size and also the grid points should be evenly distributed circumferentially. This condition can be always satisfied for full annulus calculations. When the rotating blades are moving, the mesh of the rotor blades moves with the blades. The one-to-one connection of the two grid points from the stationary blade to the moving blade at the sliding interface will remain on the same grid points when the circumferential distance of the two grid points is small. When the circumferential distance of the two grid points is greater than half of the grid interval due to the moving blades, the connection will switch to the next grid point so that all the grid points remain one-to-one connected without high mesh skewness. This process keeps being repeated in the rotor-stator sliding interface during the calculation.

For a full-annulus computation, the rotor and stator interface domains may be prohibitively large in terms of mesh size compared to blocks in other regions of the mesh (i.e. blocks around the rotor blade). This requires for interface domains to be split into smaller regions circumferentially to speed up parallel computing across the interface. Fig. 2 illustrates the algorithm of the conservative sliding BC for multiple processes at the interfaces. If the interface is defined by a single block on each side of the interface, then the send and receive commands for the mpi parallel computing procedures will have only one destination ("d1") and the BC would follow the same procedure found in [26]. Once the interface is divided further into more blocks the logics behind the destinations of the send and receive commands for mpi become increasingly more complex. The top sketches in Fig. 2 illustrate the case of having the interface divided into three congruent blocks. At time $t = 0$ all blocks are one to one where $1, 2, \ldots$ connect directly with $1', 2', \ldots$ respectively. After some time $t = \tau$ the configuration in the top to the left of the dashed line is present. The arrows show the direction of the mpi command send across the interface for the block with the corresponding color. The labels 'd1' and 'd2' represent destination 1 (the block connected one-to-one at t=0) and destination 2 (the block that follows due to rotation direction) respectively; these labels are assigned for each block based on its neighboring blocks. The blocks defined as d1 and d2 will depend on whether the current block is on the rotor side of the interface or the stator/IGV side and whether it is downstream or upstream of the interface. Assuming that $\Delta\tau = 1/(3\Omega)$, then at $t = \Delta\tau$ the blocks are again one-to-one but with block indices shifted once following the rotation direction; and at $t = \tau + \Delta\tau$ the top configuration to the right of the dashed line applies. At this moment the blocks d1 and d2 have switched since neighboring blocks have different indices. To account for this change in destination blocks for mpi send and receive, arrays with the indices of the blocks upstream and downstream of the interfaces are built such that every $\Delta\tau$ time interval the array with the downstream (red) blocks changes according to rotation convention.

The algorithm for each individual cell is shown at the bottom of Fig.2. Let the rotor domain be rotated by two cells from the initial position. Then, the cell 3 to 11 on the rotor side and the cell 1 to 9 on the stator side are matched and exchanged, while the cell 1 and 2 of the rotor domain and the cell 10 and 11 of the stator domain have no cells to exchange. Therefore, we define the exchange array of those cells to the corresponding neighboring block (i.e. 'd2'). For instance, the rotor cell 1 and 2 are rotated by the angle(ϕ) and are exchanged with the stator cell 10 and 11 of block 'd2'. We employ the conservative cell exchange technique to reduce the computational efforts and to fully conserve data exchange. The rotated mesh is located to the closest cell of the counterpart domain. When Δt is large such that the rotor mesh sliding distance is greater than one

circumferential grid cell spacing, more pseudo time steps are usually needed to reduce the residual due to the large rotor moving distance.

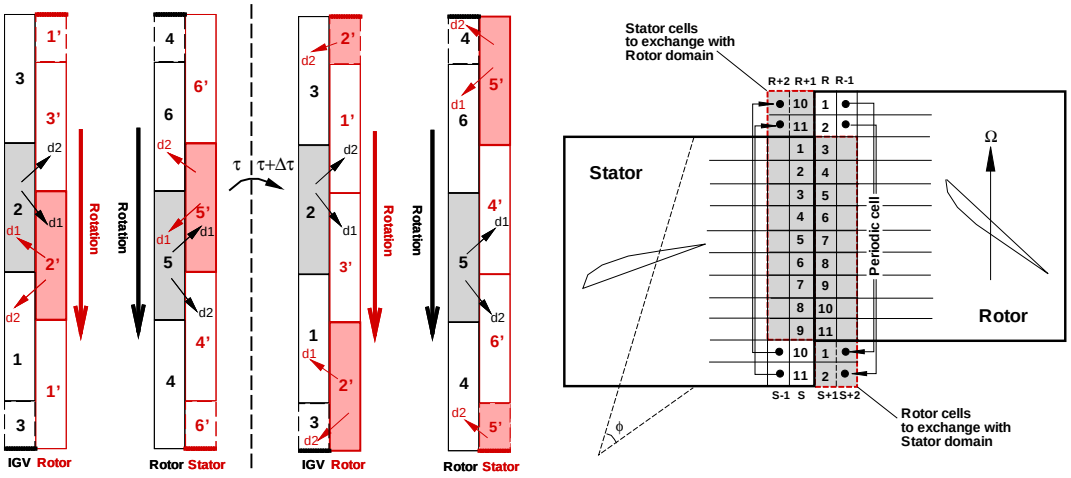

FIGURE 2: Rotor/Stator interface exchange algorithm between blocks (left) and between cells (right)

5 Computational Mesh

The full-annulus mesh for 1-1/2 stage of the compressor is presented in Fig. 3. The rotor tip clearance is modeled with 21 grid points using an O-mesh block. The mesh of IGV/rotor/stator is partitioned to total 1246 blocks for parallel computation. The grid around the blade was constructed as an O-mesh. The mesh size for the IGV and stator is 121(around blade)×101(blade-to-blade)×71(blade span); for the rotor the mesh size is 201(around blade)×101(blade-to-blade)×71(blade span). An H-mesh layer is used for the matched one-to-one grid point connection at the sliding BC interface of IGV/rotor/stator that enables variable exchange in a fully conservative manner. Each H-mesh layer has 7 blocks with a mesh size of 201(tangential)×6(axial)×71(blade span). The total mesh size for this full-annulus simulation of 1-1/2 compressor stages is 97,317,920.

6 Numerical Probes

The numerical probes to acquire the static pressure responses at the tip clearance are shown in Fig. 4. Total 60 points on a blade surface, 5 points in the middle of tip clearance and 5 points at the casing surface are mounted. The first numeral of the probe number means location around blade surface and the second numeral indicates location of blade span. For example, the probe 64 means the 6th probe from the trailing edge and the 4th probe from the hub, which is on the suction surface of 92% blade span near leading edge.

7 Results and Discussion

The rig testing of the axial compressor with 1.1% tip clearance [2] is shown to have the NSV frequency range of 2600 Hz to 2661 Hz, which is located between 12EOL(engine order line) to 13EOL as shown in the Campbell diagram in Fig. 5. The measured compressor NSV is at 2600 Hz at the present simulation operating condition of 12880 RPM. The residual is reduced by three orders of magnitude within each physical time step, which is usually achieved within 15 to 20 pseudo time step iterations. A non-dimensional time step of about 0.005 is used. Note the Campbell diagram can be used to evaluate whether a blade frequency including natural frequency is synchronous or not with engine shaft. EOL in Campbell diagram is obtained by integer multiples of rotor shaft frequency with respect to RPM. The full-annulus NSV predicted is 2513 Hz with some blades of the annulus showing a NSV of 2365 Hz and 2660 Hz. The full-annulus NSV is underpredicted by about 3.3% compared to the experiment as shown in Fig. 5.

Since NSV of axial compressors is typically observed in stable operation [1–4], steady flow simulations are conducted using a single passage of the compressor at different back pressure conditions to capture the speedline. The compressor speedline is captured to corroborate the full-annulus simulation is performed at the stable operation region far from stall

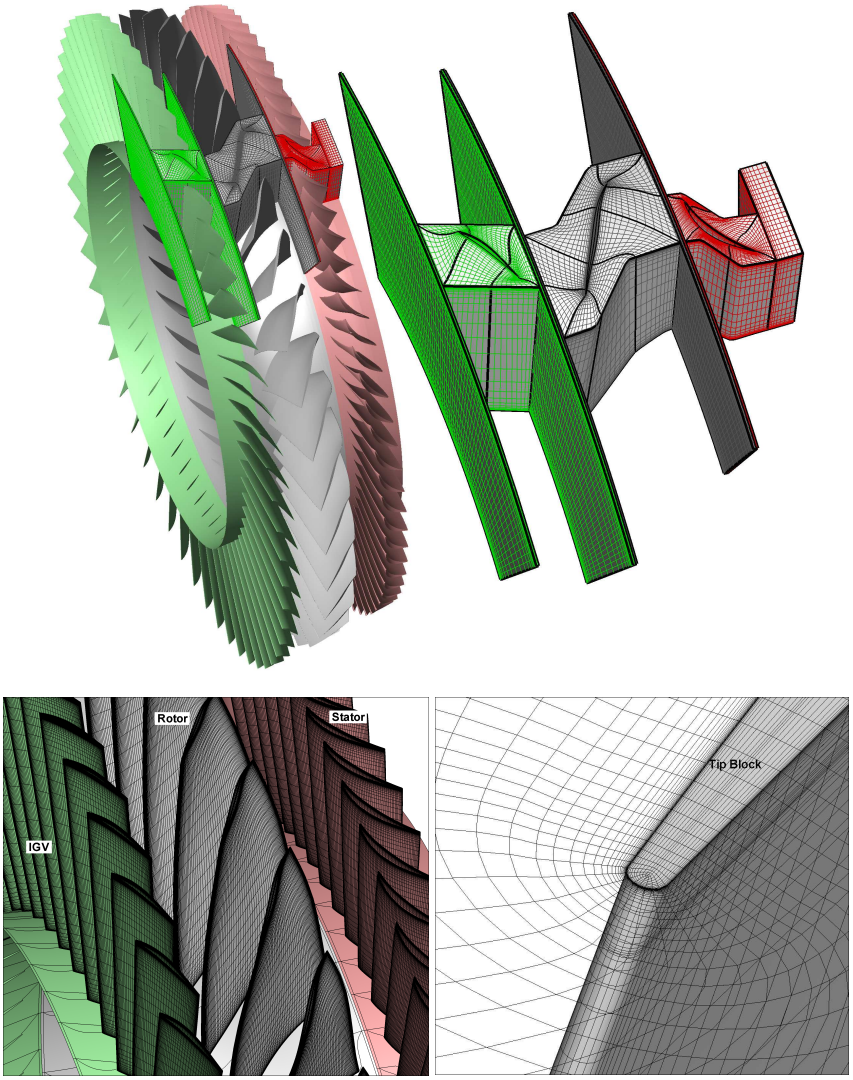

FIGURE 3: Full Annulus mesh for NSV simulation and close-up views of blade surface mesh, interface H-mesh blocks and rotor tip gap O-mesh.

region. Fig. 6 shows the predicted speedline of the 1-1/2 stage axial compressor. Note that the full-annulus speedline data in Fig. 6 are obtained by averaging the final 2 rotor revolutions to avoid the transitional period since the unsteady computations are started from the steady solutions obtained by a mixing plane approach [26].

7.1 Flow Structure and Instabilities

To ensure that the conservative sliding BC is working properly the wake propagation patterns of the 1-1/2 stage compressor is observed for 3.25 and 3.5 rotor revolutions. Fig. 7 shows the instantaneous change in entropy contours at a constant radius at 50% of the span for the aforementioned times. The IGV wakes propagate to the rotor blade row and further downstream both IGV and rotor wakes combine and propagate to the stator blade row causing the entropy increase through the stator to be much larger.

Previous unsteady simulations of the present high-speed compressor [2,10,27] have shown that a rotating instability (RI) above 78% of the span causes NSV. This near-blade-tip RI has been shown to occur in all rotor blades of the 1/7th annulus simulations [10, 27], and the present simulation shows that this instability is also present in all the blades of the full-annulus simulation as shown in Fig. 8.

The tornado-like vortex structure is shown in Fig. 9. It can be seen that the reverse flow occurs at the outer span region of the vortices. The axis of the tornado vortex, shown by the vortex core line, is perpendicular to the suction surface of the blade. When observed for the full-annulus in Fig. 10, the vortex core line of the RI for T=3.5 revolutions has a clear presence in every rotor-blade passage near and in front of the leading edge of the blades which indicates that the tornado-vortex tube is closed around the annulus. Vortex cores are almost perpendicular to the suction surface of rotor blades as shown in more

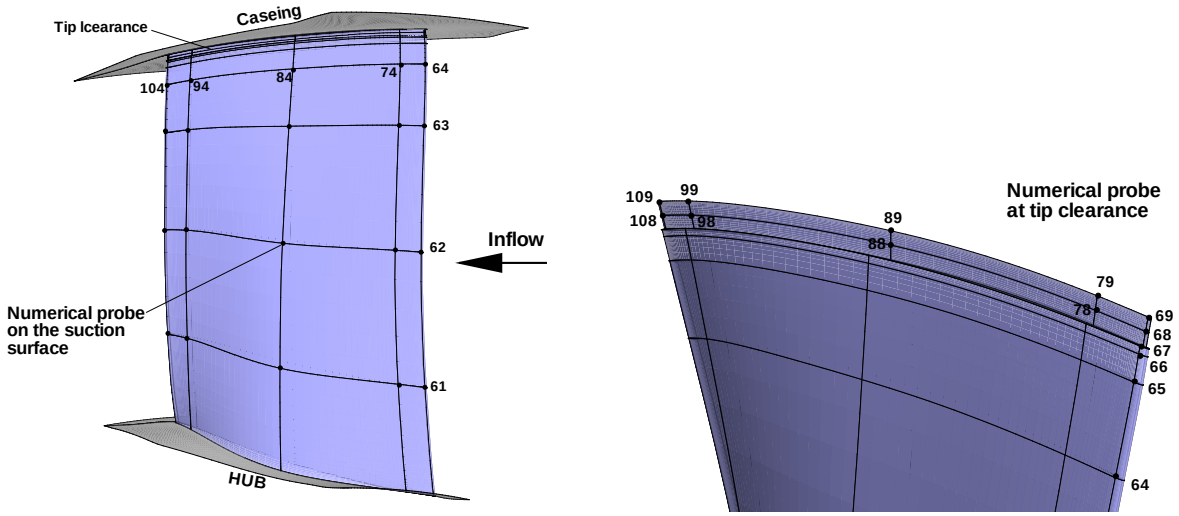

FIGURE 4: Numerical probes of the rotor blade

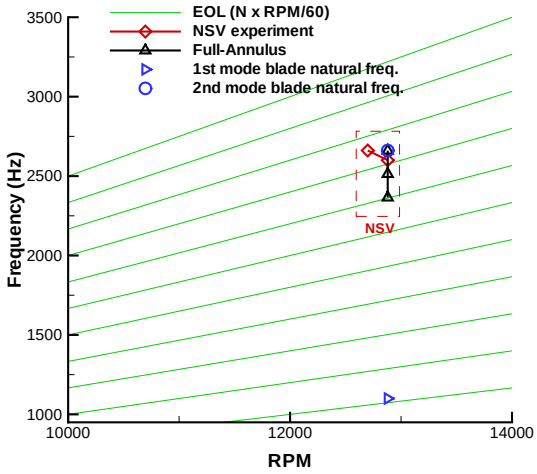

FIGURE 5: Campbell diagram

detail in Fig. 11. Also Fig. 11 shows that the RI propagation direction is parallel and opposite to the rotation direction in the relative frame. This can be further confirmed in Fig. 12 where the instantaneous tornado vortex movement over 2 rotor blades is captured. The full-annulus URANS simulates how the tornado vortex causes the NSV. The tornado vortex on the blade A suction surface at $\frac{1}{70}$ Rev moves to the blade B at $\frac{6}{70}$ Rev in the opposite direction to the rotor rotation. The tornado vortex travels fast on the suction surface of the blade and stays relatively longer at the passage outlet crossing to the next blade leading edge. Such a tornado vortex motion trajectory generates two low pressure regions due to the vortex core positions, one at the leading edge and one at the trailing edge, both are oscillating due to the vortex coming and leaving. These two low pressure regions create a pair of coupling forces that generates a torsion moment causing NSV. This is consistent with the experimental and numerical observations in [2,27] that the NSV of this rotor is dominant at its first torsion mode(2nd mode). The frequency of this tornado vortex propagation captured is roughly equal to the NSV frequency of the blade pressure signals. Other experiments [1, 4] for axial fan/compressor also show that the flow instabilities in the vicinity of rotor tip rotates circumferentially and cause NSV.

7.2 Full-Annulus NSV Frequencies

The full-annulus NSV frequency was measured and compared to a previous 1/7th annulus simulation [10] for a rotor blade geometry with a tip-to-casing gap of 1.1% of tip-chord. Fig. 13 shows the predicted frequencies for the normalized pressure signals on the blade suction surface and compares them to the frequencies predicted by the 1/7th simulation. This

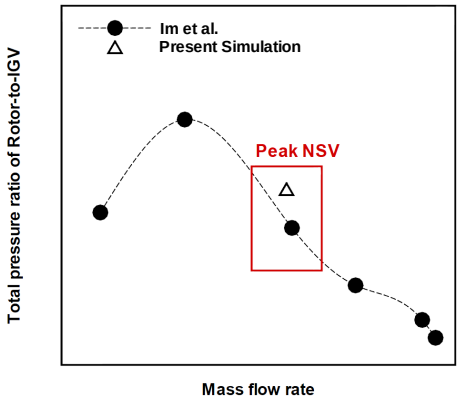

FIGURE 6: Total pressure ratio of IGV-to-Stator versus mass flow rate at the rotor exit.

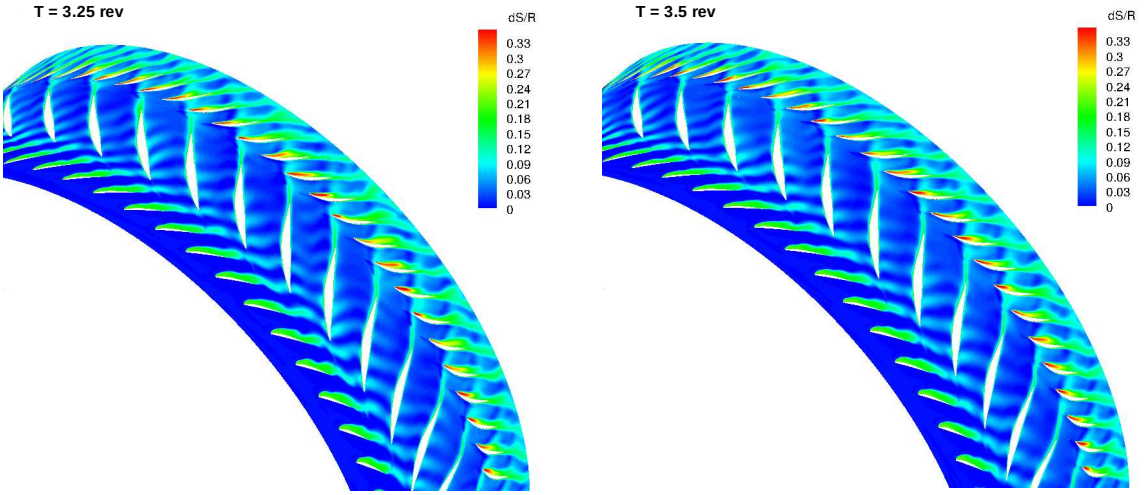

FIGURE 7: 1-1/2 Stage wake patterns shown by entropy increase contours at 50% span at 3.25 and 3.5 revolutions.

demonstrates that the circumferentially time-shifted phase-lag BC used in [10] can capture an NSV frequency of 2513 Hz, which is the same as the full-annulus NSV frequency. A sample static pressure reading of one of the 35 rotor blades is presented for the numerical probe at 78% of span at the LE (probe 63) in Fig. 14. The small zoom-in view of a pressure signal period is used to estimate its frequency, which is approximately 2525 Hz and near the computed NSV of 2513 Hz and the experimentally measured frequency of 2600 Hz, and validates the frequency analysis performed.

Fig. 15 summarizes the frequency maps of all 35 rotor blades for readings from probes at the LE of rotor blades. Upon further review of these frequencies there were two important findings that were not captured by the 1/7th simulation:

1. The dominant NSV frequency was not 2513 Hz for all blades, albeit the majority of blades did exhibit this behavior. Some blades presented different NSV frequencies of 2365 Hz and 2660 Hz.
2. The NSV frequencies were for the most part the highest peak in the frequency map, but some blades showed phenomena of lower frequency taking precedence to the NSV phenomenon as seen in Fig. 15.

The high response of frequencies well below 2500 Hz show a high incidence of separated flow through out the annulus. Comparing to experimental results in Fig. 1, measurements by the strain gages on the blades do not show this behavior, but the pressure measurements on the casing wall do show that while NSV phenomena has dominance, flow frequencies related to SFV are still significant in amplitude compared to NSV-related frequencies. The difference in these two behaviors can be explained by the nature of the measurement. Strain gage measurements follow blade deformation and therefore the dominant frequencies captured will be modal, whereas the pressure transducer will capture all frequencies found in the flow

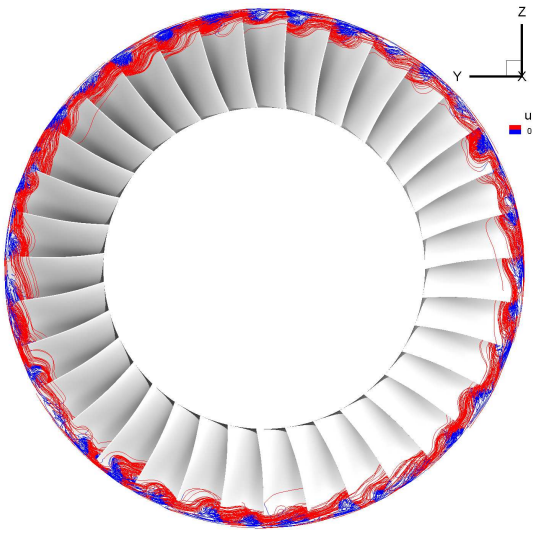

FIGURE 8: Vortex structure predicted in rotor stage above 78% span with all blades showing flow instability. Red shows flow moving downstream, blue shows backflow (inflow is into the page).

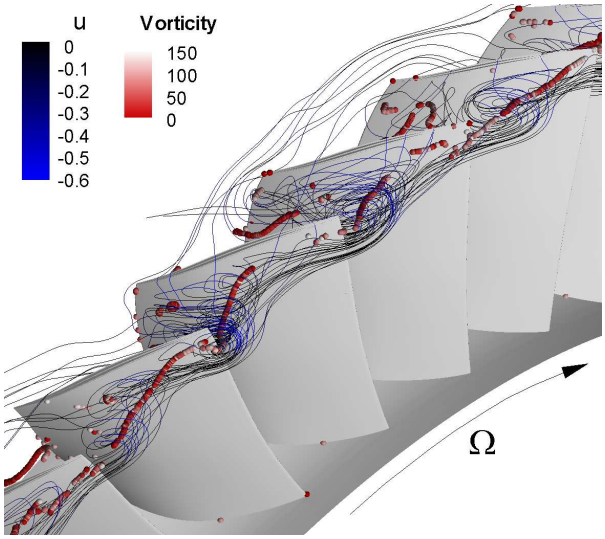

FIGURE 9: Zoom-in view of the tornado-like vortices near the tip region of rotor blades shown by streamlines colored by reverse axial velocity with vortex core shown in red.

without being influenced by blade modal frequencies. Since the numerical probes used in this simulation act more as pressure transducers and the blades are assumed to be rigid, the frequencies captured should and do behave like those captured by the pressure transducers in the experiment.

The key issue with these lower frequencies is that they hint at the presence of secondary flow features other than NSV that relate to flow separation. In Fig. 16 a tip clearance vortex travelling in a streamwise direction is present along with the tornado vortex travelling in a circumferential direction. The streamwise vortex clearly originates at the rotor blade tip whereas the circumferential vortex generates at a span of about 80%. This phenomenon also explains why SFV frequencies are more dominant at locations on the suction surface of the blade downstream of LE as shown in Fig. 17, where probe measurements are at a location 30% of tip chord downstream of LE, and in Fig. 18 with probes located at TE.

The dual-vortex system may provide some answers as to why the tornado vortex can be closed. Fig. 19 shows two instantaneous vector fields near the two vortices separated by $\Delta t = 1/70$ revolutions. The rotation direction of both vortices is opposite to each other, which means that when they interact with each other this will energize both structures. Also this interaction will cause high pressure gradients on the blade surface that will change location as the vortices propagate in their corresponding directions. This means that not just blade vibration excited by the tornado vortex will cause the NSV to sustain throughout operation, but also flow separation near the tip region will have an influence. Since this simulation assumed rigid blades, a closer look at the blade vibration with flow separation should be performed to determine the influence of flow

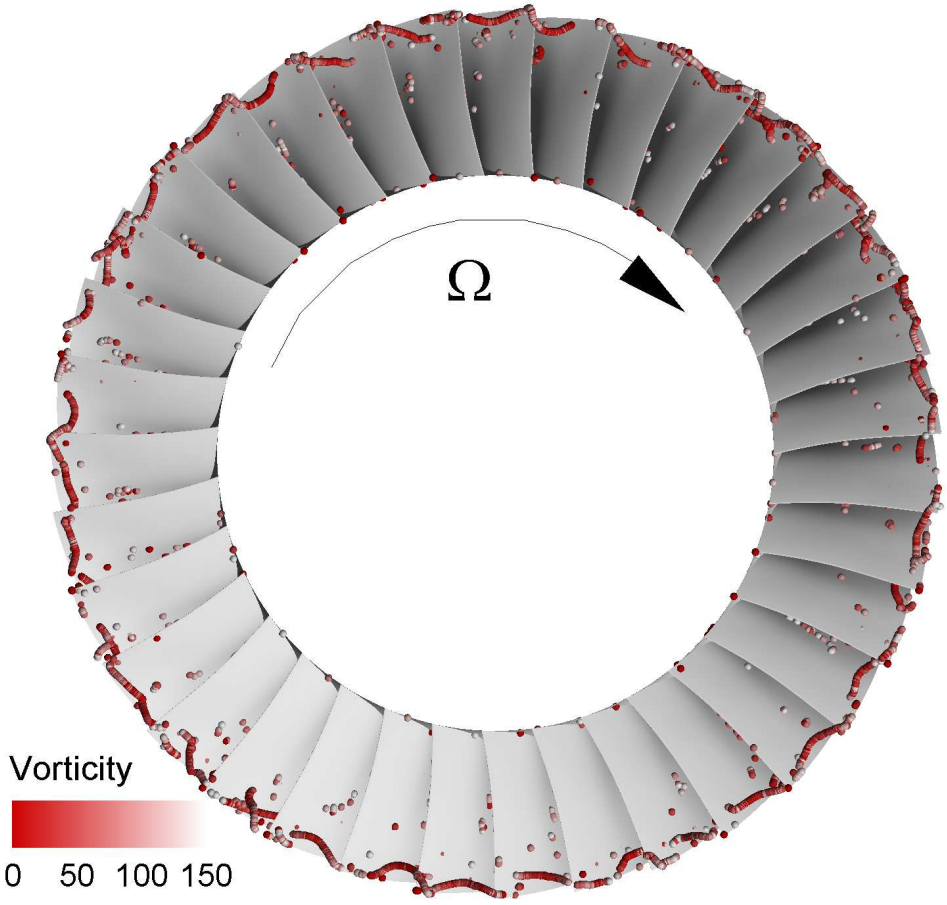

FIGURE 10: Instantaneous vortex core structure predicted at T=3.5 rev. with all blades showing presence of vortical flow showing that the vortex tube is closed.

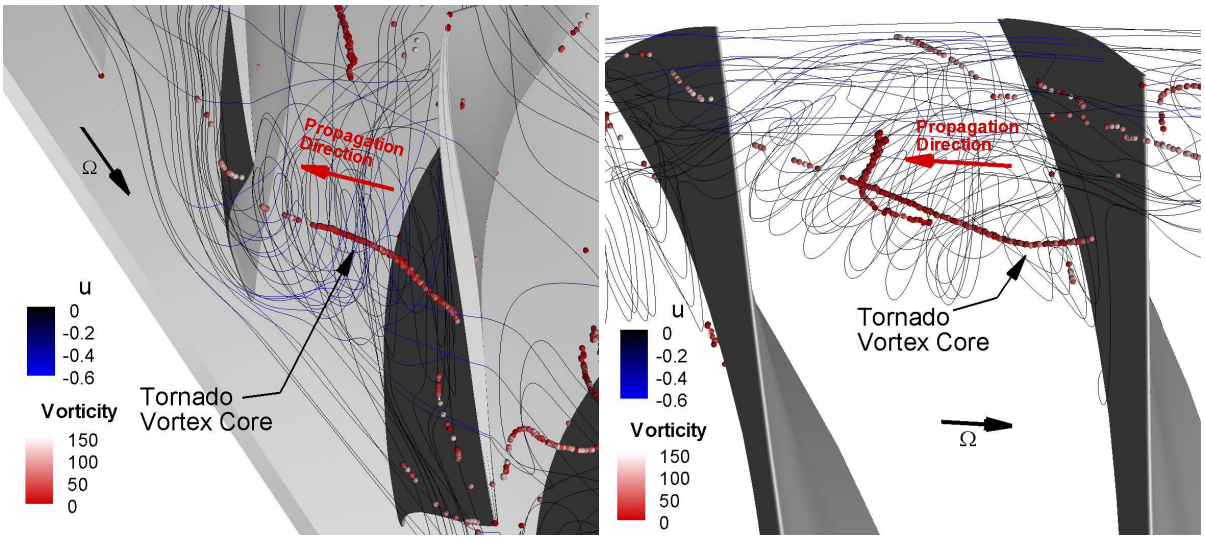

FIGURE 11: Side and top view of a tornado vortex with vortex core almost perpendicular to suction surface and propagation direction parallel but opposite to rotation direction.

separation with circumferentially propagating vortices.

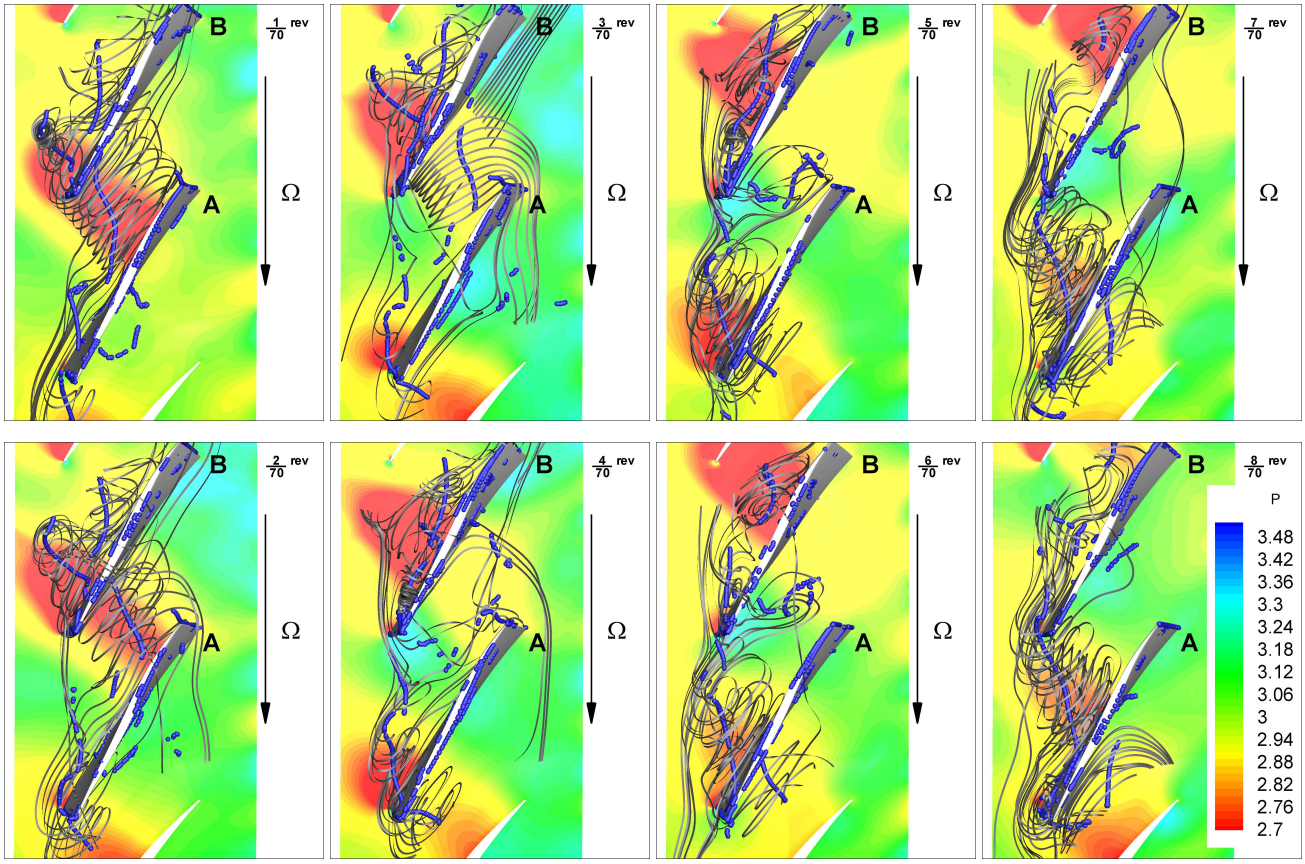

FIGURE 12: Instantaneous vortex trajectories in tip region every 1/35th of a revolution colored by the normalized static pressure.

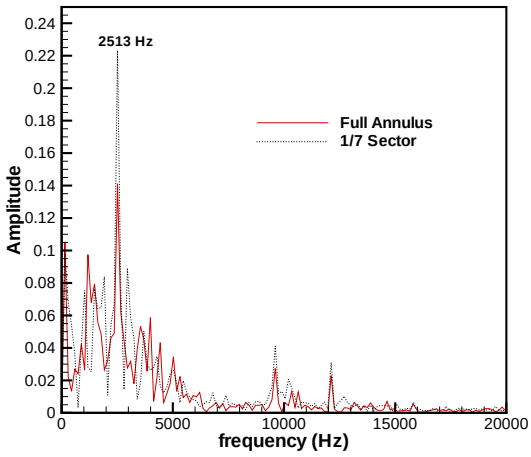

FIGURE 13: Predicted NSV frequencies for full annulus and 1/7th annulus simulations at probe 64 for a sample blade.

8 Conclusion

A 1-1/2 stage high-speed compressor was simulated using a full-annulus configuration to minimize BC effect on solution. A URANS solver was used to capture the NSV flow excitation frequency of 2513 Hz which is 3.3% underpredicted compared to experimental data. The phenomena observed matches for the most part to that observed for 1/7th annulus URANS simulation using a circumferential time-shifted phase-lag BC. It is shown that the tornado vortex formed in the vicinity of the rotor tip propagates at the speed of a non-engine order frequency and causes the NSV. The tornado vortex

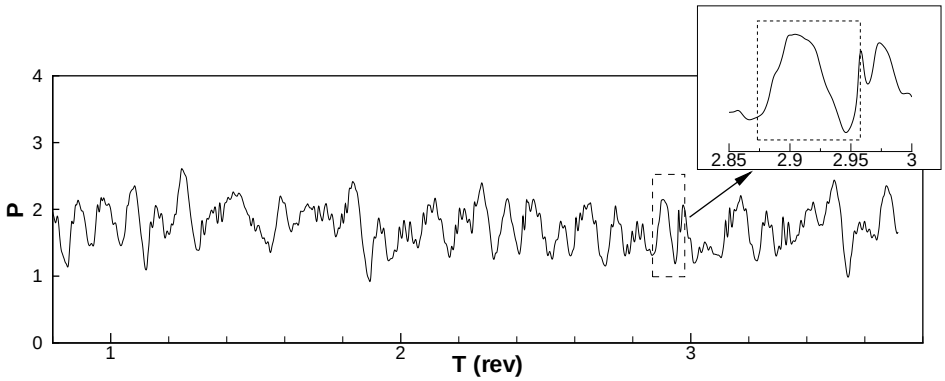

FIGURE 14: Pressure signal for sample blade of full-annulus (blade 3) at probe 63 with zoom-in of a signal period with an approximate frequency of 2525 Hz.

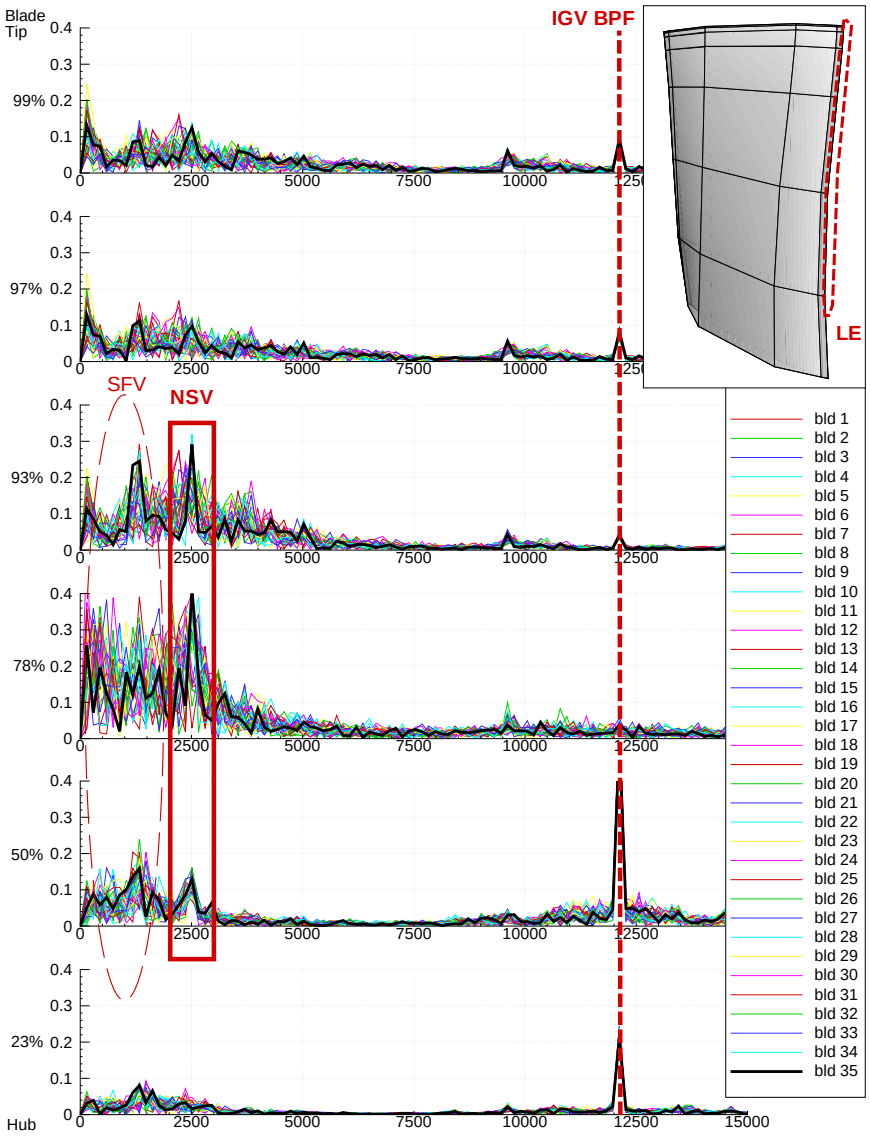

FIGURE 15: Frequency maps for all 35 rotor blades for LE probes showing strong frequency response for NSV frequency of 2513 Hz.

travels fast on the suction surface of the blade and stays relatively longer at the passage outlet crossing to the next blade

leading edge. Such a tornado vortex motion trajectory generates two low pressure regions due to the vortex core positions, one at the leading edge and one at the trailing edge, both are oscillating due to the vortex coming and leaving. These two low pressure regions create a pair of coupling forces that generates a torsion moment causing NSV.

The full-annulus simulation shows that the tornado vortex structure is consistent throughout the whole annulus, but the NSV frequency varies for some blades to 2365 Hz and 2660 Hz. Also, frequencies below the NSV excitation frequency of 2513 Hz with large amplitudes in response point at flow-separation related phenomena being present. This behavior is consistent with experimental measurements but was not observed as prominently in the 1/7th simulation. Further study of the flow showed that the blade passages have a dual-vortex system where both streamwise-propagating tip clearance vortices and circumferentially-propagating tornado vortices interact, and their interaction may also be a mechanism that strengthens the tornado vortex causing NSV.

The influence of flow separation as an important mechanism that sustains NSV in compressor blades must be checked with interaction of structure vibration. It appears that only full-annulus simulations can take into account this effect. Since the present full-annulus simulation assumes rigid blades, future work should include a full-annulus simulation with vibrating blades to determine the influence of blade modal frequencies coupling with flow frequencies and how this fluid-structure interaction affects NSV.

Acknowledgement

We greatly appreciate "LC" Colmenero and Steve Manwaring at GE Aviation for providing feedback and support. The grants support from AFRL and the industrial partners of GUIde Consortium, 10-AFRL-1024 and 09-GUIDE-1010, are acknowledged. The numerical simulations are conducted at the Center for Computational Sciences at the University of Miami and Air Force Research Lab DoD Supercomputing Resource Centers.

REFERENCES

[1] M. Baumgartner, F. Kameier, and J. Hourmouziadis, "Non-Engine Order Blade Vibration in a High Pressure Compressor." ISABE, Twelfth International Symposium on Airbreathing Engines, Melbourne, Australia, 10-15, 1995.

[2] R. Kielb, J. Thomas, P. barter, and K. Hall, "Blade Excitation by Aerodynamic Instabilites - A Compressor Blade Study." ASME Paper No. GT-2003-38634, 2003.

[3] J. Marz, C. Hah, and W. Neise, "An Experimental and Numerical Investigation Into the Mechanisms of Rotating Instability," *Journal of Turbomachinery*, vol. 124, pp. 367–375, 2002.

[4] R. Mailach, I. Lehmann, and K. Vogeler, "Rotating Instabilites in an Axial Compressor Originating From the Fluctuating Blade Tip Vortex." ASME Paper No. GT-2003-38634, 2003.

[5] J. Thomassin, H. Vo, and N. Mureithi, "Blade Tip Clearance Flow and Compressor Nonsynchronous Vibrations: The Jet Core Feedback Theory as the Coupling Mechanism," *Journal of Turbomachinery*, vol. 131, pp. 11013–1–11013–9, 2009.

[6] J. Thomassin, H. Vo, and N. Mureithi, "The Tip Clearance Flow Resonance Behind Axial Compressor Nonsynchronous Vibration," *Journal of Turbomachinery*, vol. 133, pp. 041030–1–041030–10, 2011, doi:10.1115/1.4001368.

[7] A. Sanders, "Nonsynchronous Vibration(NSV) due to a Flow-Induced Aerodynamic Instability in a Composite Fan Stator," *Journal of Turbomachinery*, vol. 127, pp. 412–421, 2005.

[8] Vo, H.D., "Role of Tip Clearance Flow in Rotating Instabilities and Nonsynchronous Vibrations," *Journal of Propulsion and Power*, vol. 26, pp. 556–561, doi: 10.2514/1.26709, 2010.

[9] S. Clark, R. Kielb, and K. Hall, "Developing a Reduced-Order Model to Understand Nonsynchronous Vibration (NSV) in Turbomachinery." ASME GT2012-68145, 2012.

[10] H.S. Im, and G.C. Zha, "Effects of Rotor Tip Clearance on Non-Synchronous Blade Vibration for an Axial Compressor." ASME GT2012-68148, 2012.

[11] J. Chen, M. Hathaway, and G. Herrick, "Prestall Behavior of a Transonic Axial Compressor Stage via Time-Accurate Numerical Simulation," *AMSE J. of Turbomach.*, vol. 130, pp. 1–12, doi:10.1115/1.2812968, 2008.

[12] C. Hah, J. Bergner, and H. Schifer, "Short Length Scale Rotating Stall Inception in a Transonic Axial Compressors : Criteria and Mechanisms." GT2006-90045, ASME Turbo Expo, 2006, doi:10.1115/GT2006-90045.

[13] H.S. Im, X.Y. Chen, and G.C. Zha, "Detached Eddy Simulation of Stall Inception for a Full Annulus Transonic Rotor," *Journal of Propulsion and Power*, vol. 28 (No. 4), pp. 782–798, doi: 10.2514/1.58970, 2012.

[14] H. Khaleghi, M. Boroomand, A.M. Tousi, and J.A. Teixeira, "Stall Inception in a Transonic Axial Fan," *Journal of Power and Energy*, vol. 222, pp. 199–208, doi:10.1243/09576509JPE407, 2008.

[15] F. Lin, J. Zhang, J. Chen, and C. Nie, "Flow Structure of Short-Length-Scale Disturbance in an Axial-Flow Compressor," *Journal of Propulsion and Power*, vol. 24, pp. 1301–1308, doi: 10.2514/1.36525, 2008.

[16] P.R. Spalart, W.H. Jou, M. Strelets, and S.R. Allmaras, "Comments on the Feasibility of LES for Wings, and on a Hybrid RANS/LES Approach." Advances in DNS/LES, 1st AFOSR Int. Conf. on DNS/LES, Greyden Press, Columbus, H., Aug. 4-8, 1997.

[17] G.C. Zha, Y.Q. Shen, and B.Y. Wang, "An Improved Low Diffusion E-CUSP Upwind Scheme ," *Journal of Computer and Fluids*, vol. 48, pp. 214–220, 2011, doi:10.1016/j.compfluid.2011.03.012.

[18] Y.Q. Shen, G.C. Zha, and B.Y. Wang, "Improvement of Stability and Accuracy of Implicit WENO Scheme," *AIAA Journal*, vol. 47, pp. 331–334, DOI:10.2514/1.37697, 2009.

[19] Y.Q. Shen, B.Y. Wang, and G.C. Zha, "Implicit WENO Scheme and High Order Viscous Formulas for Compressible Flows ." AIAA Paper 2007-4431, 2007.

[20] B. Wang, Z. Hu, and G. Zha, "A General Sub-Domain Boundary Mapping Procedure For Structured Grid CFD Parallel Computation," *AIAA Journal of Aerospace Computing, Information, and Communication*, vol. 5, pp. 425–447, 2008.

[21] M. Rai, "Three-dimensional Navier-Stokes Simulations of Turbine Rotor-Stator Interaction. I - Methodology ," *AIAA Journal of Propulsion and Power*, vol. 5, pp. 305–311, 1989.

[22] M.B. Giles, "Stator/Rotor Interaction in a Transonic Turbine," *AIAA Journal of Propulsion and Power*, vol. 6, pp. 621–627, 1990.

[23] L. He, "Three-Dimensional Unsteady Navier-Stokes Analysis of Stator-Rotor Interaction in Axial Flow Turbines," *Proceedings of the Institution of mechanical Engineers, Part A: Journal of Power and Energy*, vol. 214, pp. 13–22, 2000.

[24] A. Ruprecht, C. Bauer, C. Gentner, and G. Lein, "Parallel Computation of Stator-Rotor Interaction in an Axial Turbine." ASME PVP Conference, CFD Symposium, Boston, 1999.

[25] J.P. Chen, and J.W. Barter, " Comparison of Time-Accurate Calculations for the Unsteady Interaction in Turbomachinery Stage." AIAA Paper 98-3292, 1998.

[26] H.S. Im, X.Y. Chen, and G.C. Zha, "Simulation of 3D Multistage Axial Compressor Using a Fully Conservative Sliding Boundary Condition." ASME IMECE2011-62049, International Mechanical Engineering Congress & Exposition, Denver, November 2011, 2011.

[27] H.S. Im, and G.C. Zha, "Simulation of Non-Synchronous Blade Vibration of an Axial Compressor Using a Fully Coupled Fluid/Strcuture Interaction." ASME GT2012-68150, 2012.

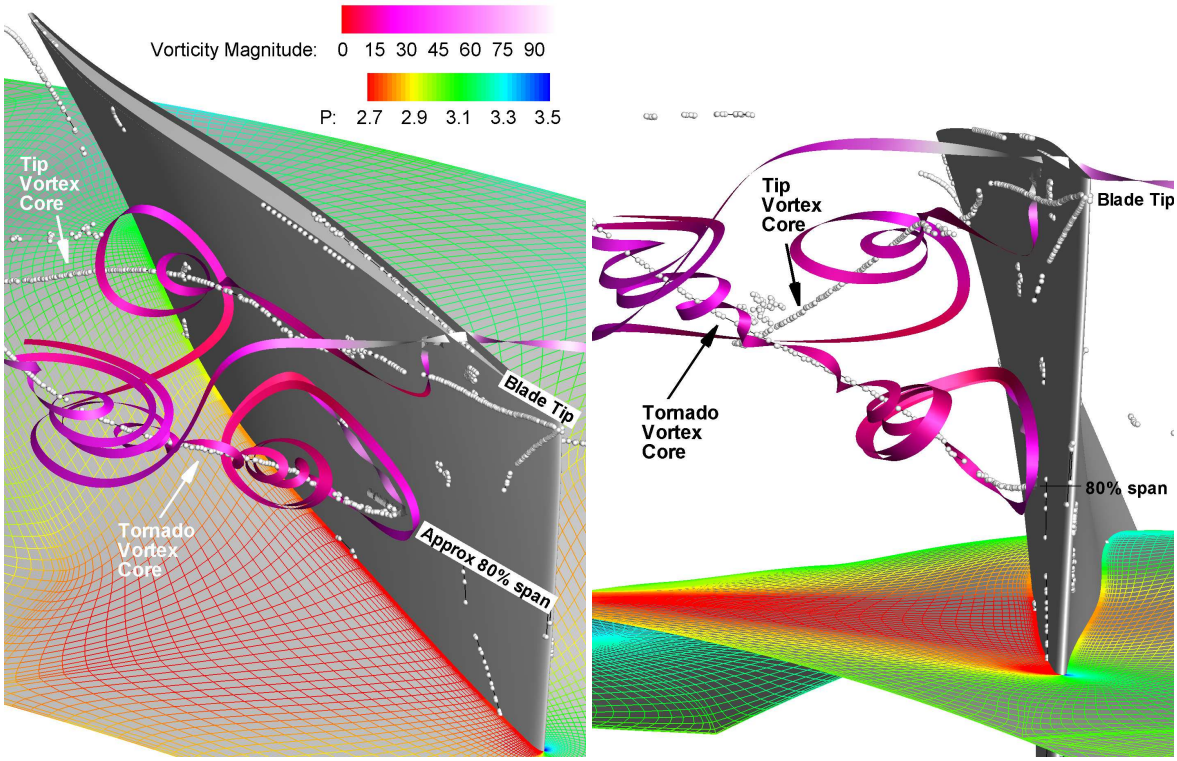

FIGURE 16: Instantaneous flow and vortex tracking showing streamwise-travelling tip vortex interacting with circumferentially-travelling tornado vortex.

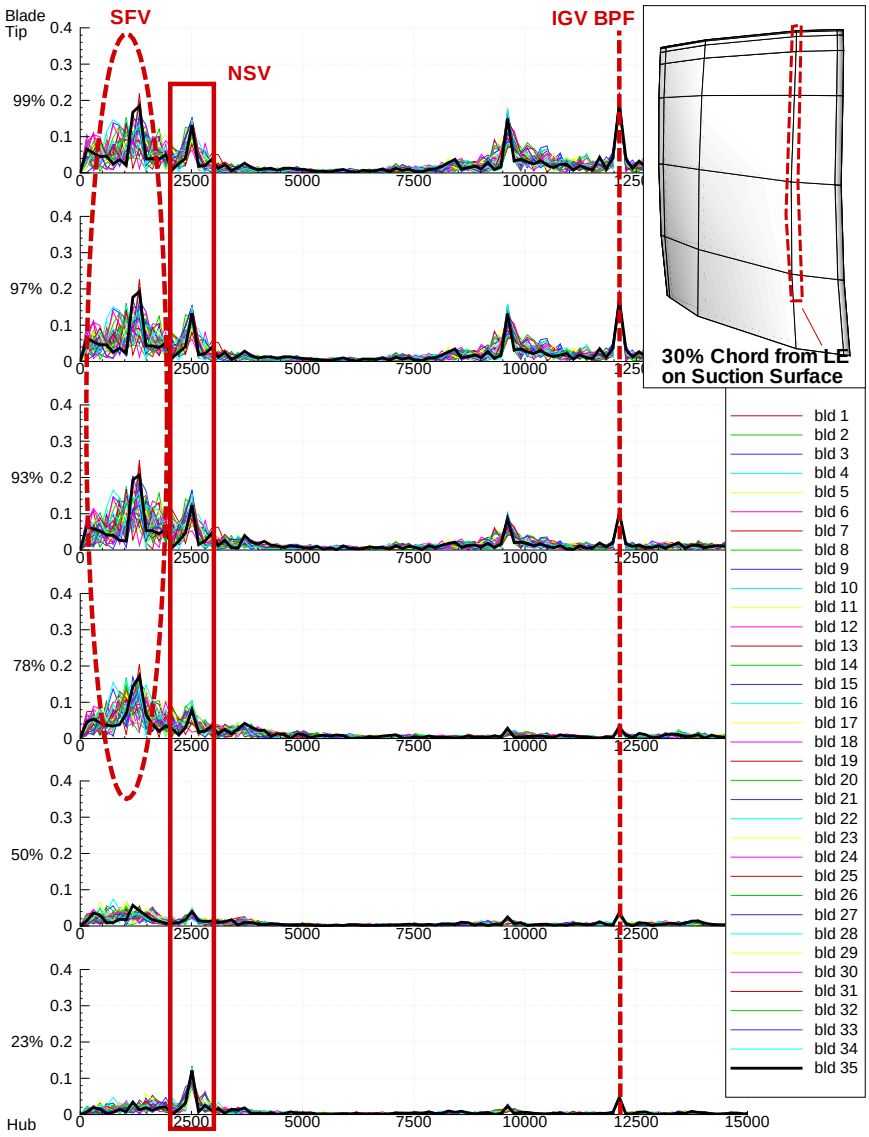

FIGURE 17: Frequency maps for rotor blade probes downstream of LE on suction surface by 30% of tip chord showing frequency response for NSV and SFV.

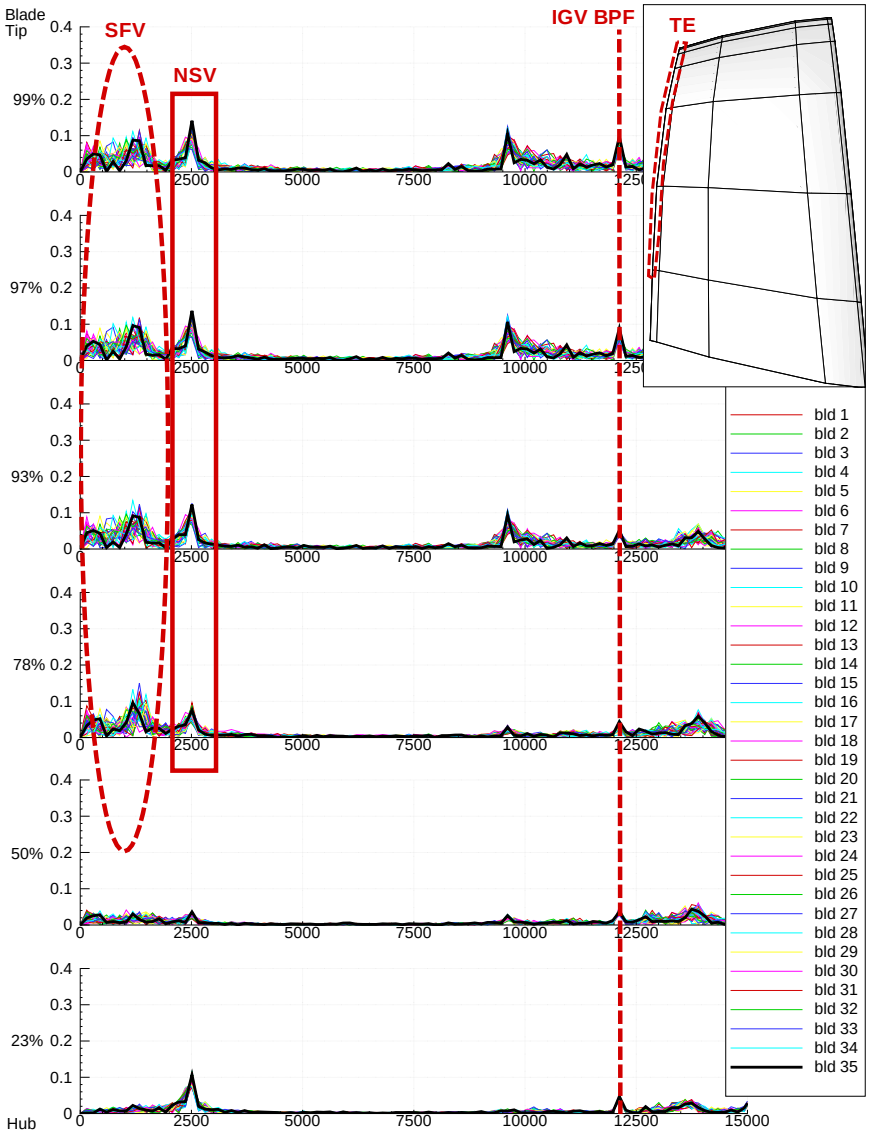

FIGURE 18: Frequency maps for rotor blade probes at TE showing strong frequency response for SFV with some NSV.

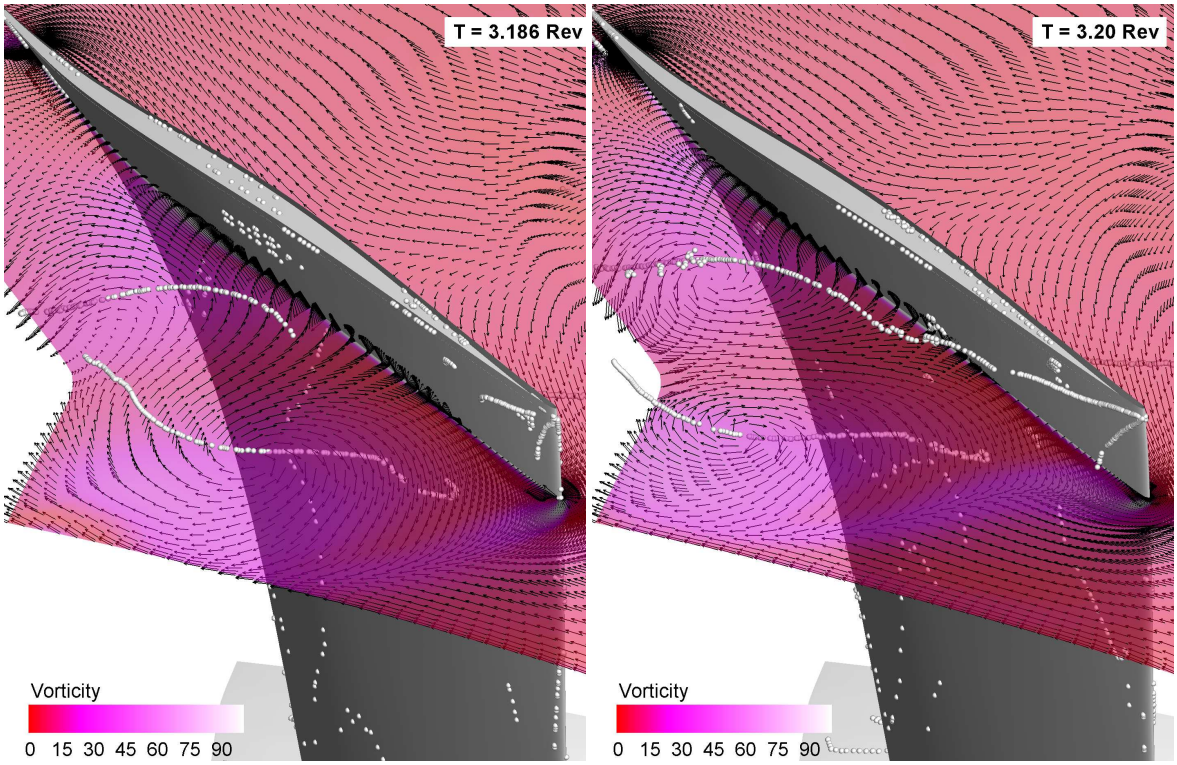

FIGURE 19: Velocity vectors showing dual-vortex system interaction where vortices rotate in opposite directions amplifying each other.